Published in Applied Surface Science 270:675-684, 2013

Combined modification of a TiO_2 photocatalyst with two different carbon forms

Alejandro Ansón-Casaos*, Ignacio Tacchini, Andrea Unzue, M. Teresa Martínez
Instituto de Carboquímica ICB-CSIC, Miguel Luesma Castán 4, 50018 Zaragoza, Spain

*Corresponding author: E-mail: alanson@icb.csic.es
Tel.: +34 976 733977

Abstract

Hydrothermally synthesized titanate nanotubes were carbon-doped through a thermal treatment in the presence of glucose followed by blending with single-walled carbon nanotubes (SWCNTs). A series of TiO_2-based materials was prepared with various initial glucose contents and two SWCNT types, resulting in total carbon contents from 0.3 wt.% to nearly 26 wt.%. Electron microscopy observations indicated that titanate nanotubes were converted into nanorods during the thermal treatment, and X-ray diffraction patterns confirmed that all the treated materials mostly consisted of anatase TiO_2. Glucose pyrolisis caused changes in the infrared and X-ray photoelectron spectra of the titania material, indicating an interaction between the inserted carbon atoms and titanium atoms. Raman spectra of SWCNT/C/TiO_2 hybrids showed characteristic bands of both the SWCNT and anatase TiO_2 phases. SWCNT/C/TiO_2 multicomponent materials demonstrated substantially better photocatalytic activities than P25 TiO_2 for methylene blue degradation under visible light irradiation. Independently from its origin, the presence of carbon caused a strong increase in the TiO_2 visible light absorption. However, the results obtained with the C/TiO_2 and SWCNT/C/TiO_2 photocatalysts clearly showed different photocatalysis mechanisms depending on the carbon form.

Keywords: Titanium dioxide; nanorod; carbon nanotubes; nanocomposite; photocatalysis; visible.

1. Introduction

TiO_2 is one of the most promising photocatalysts due to its high reactivity under UV excitation and high photochemical stability. Moreover, the incorporation of carbon into TiO_2 materials allows the synthesis of photocatalysts with improved efficiency and activity under visible light [1]. The extension of TiO_2 absorption towards the visible region is required for practical applications that utilize solar light or artificial visible light. Many different C/TiO_2 hybrid photocatalysts have been studied, including C-doped TiO_2, TiO_2 supported on carbon materials, carbon nanostructures embedded in TiO_2 and C-coated TiO_2 [2]. The photochemical performance of each C/TiO_2 hybrid is determined by its particular bulk, surface and interface characteristics. Even the photocatalytic mechanisms depend on the components and the preparation method of the C/TiO_2 materials.

The performance of ternary $C/C/TiO_2$ photocatalysts, made of titania and two carbon forms, have not been explored so far, except for a recent article about the photocatalytic activity of a C-doped TiO_2 coating on multi-walled carbon nanotubes (MWCNTs) [3]. Here we study a ternary $C/C/TiO_2$ nanocomposite which was prepared by thermal treatment of titanate nanotubes/glucose mixtures, followed by blending with either pristine or oxidized single-walled carbon nanotubes (SWCNTs).

Thermal treatment of titanium oxides in the presence of a carbon precursor is often applied for the synthesis of C/TiO_2 materials. Previously to our research, ethanol vapor was utilized as the carbon source for the synthesis of C-doped TiO_2 nanorods from titanate nanotubes [4]. In addition to adsorption of organic vapors, impregnation with solutions of low molecular weight carbohydrates allows a homogeneous insertion of the carbon precursor in the bulk titanium oxide. Several methods for the preparation of C/TiO_2 from glucose and sucrose can be found in the literature [5-7].

Substantial improvements in the TiO_2 photocatalytic activity have been achieved with mixtures of TiO_2 and MWCNTs [8-19], SWCNTs [20-22] or graphene [23]. Due to their availability, MWCNTs have been widely studied, even though SWCNTs and graphene are expected to have a better performance [20, 24]. These carbon nanomaterials typically act as electron acceptors and conductors, increasing the separation of the photogenerated electron/hole pairs, and thus the photocatalytic efficiency [14]. Moreover, some CNT/TiO_2 and $graphene/TiO_2$ photocatalysts also demonstrate substantial activity under visible light, indicating that carbon nanomaterials could act as sensitizers or carbon-doping sources [10]. This phenomenon seems to be

related to a chemical interaction between the carbon nanostructure and the TiO_2 phase [22].

Some ternary hybrid photocatalysts have been previously studied. Anionic codoping, for example N/F-TiO_2 or N/F- and C/N-$ZnWO_4$, has been suggested to efficiently decrease the semiconductor photoexcitation energy [25]. Coupled semiconductors, such as CdS/TiO_2/WO_3 [26] or SnO_2/ZnO/TiO_2 [27] provide cascadal transfer paths for the photoexcited electrons. The design of complex photocatalysts is an open field that provides many unexplored possibilities. In the present article, we report the characterization of ternary SWCNT/C/TiO_2 photocatalysts and we demonstrate that it is possible to merge the benefits of both glucose pyrolysis and SWCNT blending to obtain a material with improved photocatalytic properties. The carbon content was optimized to achieve high efficiencies in the decomposition of methylene blue under visible light. The comparison of activity tests for several SWCNT/C/TiO_2 and C/TiO_2 materials with different compositions reflects the fact that the photocatalytic mechanism depends on the carbon form. Some of our results confirm those previously reported for a C-TiO_2/MWCNT system [3], in spite of having a completely different synthetic approach.

2. Material and methods

2.1. Synthesis of C/TiO_2 nanorods

Titanate nanotubes (TiNTs) were synthesized following the hydrothermal method reported by Kasuga [28]. Briefly, 10 g of anatase TiO_2 particles (Aldrich, >99%, -325 mesh) was added to a 10M NaOH aqueous solution and was treated for 24 h at 135°C in a Teflon-sealed autoclave. The product was washed with 0.1M HCl, rinsed with water until pH=7, and dried for 3 h at 110ºC in an oven.

Glucose (anhydrous, 96% Aldrich) was used as the carbon source for doping. Approximately 1 ml of different concentrations of glucose solutions in water (50, 100, 200, 400, or 800 mg/ml) was added to 1g of TiNTs (BET surface area ~ 300 m^2/g, total pore volume ~ 1 cm^3/g at relative pressure $p/p^0 = 0.6$). Then, the samples were dried in an oven at 110ºC and were heated for 1 h at ~ 410ºC under a N_2 flow in a horizontal quartz reactor. As prepared samples are hereafter labeled “nG-TiNR”, where “n” stands for the amount (mg) of glucose precursor added to the TiNRs.

2.2. Preparation of SWCNT dispersions

SWCNTs were produced by the arc discharge method utilizing graphite electrodes and Ni/Y catalysts (2/0.5 atomic %) [29]. Dispersions of SWCNTs were prepared in a 1% (wt/v) aqueous solution of sodium dodecylbenzene sulfonate (SDBS), which is an anionic surfactant that has been widely used to disperse and debundle SWCNTs [30, 31]. Batches of ~ 200 mg of the pristine SWCNT sample (P-SWCNTs) were mixed with 50 mL of 1% SDBS, sonicated for 30 min with a UP 400S Hielscher tip, and centrifuged for 30 min at 13,000 rpm (23000g) in a Hermle Z387 centrifuge. The supernatant dispersion was decanted, and utilized for the preparation of hybrid photocatalysts. Centrifugation of the SDBS solution improves the SWCNT dispersion purity, decreasing the amount of metallic particles, graphite, and amorphous carbon [29].

Further purification of the P-SWCNT sample was carried out by air oxidation and acid treatment in HCl. In a typical experiment, 1g of P-SWCNTs was treated at 350ºC for 2h in an oven, refluxed in 3M HCl for 4h, filtered through a 3.0 μm polycarbonate membrane, washed with water until pH ~ 7, and dried in an air oven. The total yield of the oxidative-acid treatment was 79.5 wt%. Batches of ~ 265 mg of the oxidized SWCNT sample (Ox-SWCNTs) were sonicated, centrifuged twice in 50 mL of 1% SDBS and decanted.

The purity of the resulting SWCNT dispersions was evaluated by near-infrared spectroscopy (Bruker Vertex 70 spectrometer), following the procedure reported by Itkis et al. [32]. The purity ratio, which is a relative measurement of the content in SWCNTs and carbonaceous impurities, is defined as the background-subtracted area of the SWCNT band transition at 7750-11750 cm^{-1} divided by the total band area [32]. Purity ratios for the P-SWCNT and Ox-SWCNT dispersions were 0.078 and 0.170 respectively.

2.3. Synthesis of SWCNT/C/TiO_2 nanorod composites

Approximately 800 mg of the C/TiO_2 nanorod samples (50G-TiNR or 100G-TiNR) were sonicated in 50 mL of isopropanol for 10 min. Then, the suspension was mixed with an appropriate volume (~ 200mL) of the SWCNT dispersions (P-SWCNTs or Ox-SWCNTs in 1% SDBS), and the mixture was magnetically stirred for 24 h. The resulting product was filtered, rinsed with water, and dried in an oven at 110ºC.

2.4. Characterization techniques

The morphology of the nanostructures was studied by transmission electron microscopy (TEM, JEOL-200FXII). For TEM sample preparation, a small amount of the samples was sonicated in ethanol and placed onto Lacey microscopy grids. Surface composition, particularly carbon content, was determined by energy dispersive spectroscopy (EDS, Hitachi S3400N). Specific surface area of the powder samples was calculated from nitrogen adsorption data (Micromeritics ASAP 2020).

Crystal structure was determined by powder X-ray diffraction (XRD, Bruker AXS D8 Advance diffractometer) using CuKα radiation. The crystallite size was calculated from XRD patterns applying the Scherrer equation. Additional data of the titanium oxide crystal structure was obtained by micro-Raman spectroscopy (HORIBA Jobin Ybon spectrometer, model HR 800 UV). A green laser at 532 nm was employed for the measurements.

The interaction between carbon and TiO_2 in the composite photocatalysts was characterized by infrared spectroscopy (IR, Bruker Vertex 70 spectrometer) and X-ray photoelectron spectroscopy (XPS, ESCAPlus Omicron, Mg anode working at 1253.6 eV, 150W). For IR measurements, small amounts of the samples were mixed with spectroscopic KBr and pressed to form pellets. For XPS, the powder materials were set on copper tape, and previously to the XPS measurement, an ion gun sputtering (Ar^+, 3000V, 15mA) was applied for 2 min.

Optical properties of the powder samples were studied by UV-Visible spectroscopy. The spectrometer (Shimadzu UV-3600) was equipped with a Labsphere diffuse reflectance accessory to allow powder measurements.

2.5. Photocatalytic activity assessment

Photocatalysis experiments were carried out in a 1-litre cylindrical quartz reactor (diameter = 12 cm) with two flow valves (air entrance and purge) and a sample collector. Illumination was provided by two 8W cylindrical Hitachi Daylight lamps (30 x 1.5 cm). The lamps were located inside the reactor cylinder with a 7 cm separation between their centers (3.5 cm separation from the reactor cylinder axis). The emission spectrum of the fluorescent lamps ranges from 300 to 750 nm, with intense lines at 313, 366, 405, 435, 480, 544 and 577 nm. Polymeric STEM filters (413T10) were utilized to cover the Daylight lamps, eliminating UV radiation ($\lambda < 400$ nm). According to the

provider specifications, the 413T10 film is transparent to visible light, while most of the UV light is captured.

In a typical experiment, 300 ml of a 5 ppm methylene blue aqueous solution was introduced into the reactor with 300 mg of the tested photocatalyst. The mixture was magnetically stirred at 250 rpm in darkness for 2 hours to assure the saturation of the catalyst surface with the dye. The mixtures were subsequently aerated and illuminated. Samples of 3 mL were regularly extracted and filtered, and the dye degradation was determined by measuring the optical absorbance at 662 nm (Shimadzu UV-3600). The authors have previously reported that the color loss occurring during the experiments was mostly related to the complete mineralization of the dye [33].

3. Results and discussion

3.1. Nanoscale morphology and surface area

Figure 1 shows TEM images of various powder samples that represent subsequent stages in the preparation of SWCNT/C/TiO_2 materials. First, titanate nanotubes (TiNTs, Figure 1.a) were obtained after alkaline hydrothermal treatment of the anatase TiO_2 precursor. The inner and outer diameters of the TiNTs are around 4 nm and 10 nm respectively, and are uniform through the sample. In contrast, TiNT lengths are quite heterogeneous, ranging from approximately 50 nm to more than 500 nm. It can be observed that some nanotubes are individualized, while some others are joined longitudinally, forming bundles of thicker than 100 nm.

When TiNTs are thermally treated at 410ºC, the nanoscale morphology changes and nanorods (TiNRs, Figure 1.b) are formed, as it has been previously described [4]. TiNRs do not show central channels, and their outer diameters are in the range of 15-20 nm. Apparently, several nanotubes merge during the thermal treatment to form the nanorods. Though some TiNRs reach lengths of ~1 μm, they do not constitute continuous crystalline structures. Actually, TiNRs are formed by aggregates of smaller domains, which often separate from the nanorod structure, as it will be discussed below. As for pure TiO_2 nanorods (Figure 1.b), the result of thermally treating TiNTs in the presence of glucose is their conversion into nanorods (Figure 1.c). Table 1 includes the amount of carbon that remained in the TiO_2 materials after the treatment with glucose.

TEM images of the SWCNT/C/TiO_2 materials (Figure 1.d) demonstrate the presence of SWCNT bundles, carbon-modified TiO_2 nanorods and TiO_2 particles. Thus, the process for the preparation of SWCNT/C-TiO_2 hybrids also generates short TiO_2 nanorods and

particles with different shapes. This fact has been previously observed [34], although the total disruption of the nanorods to produce TiO_2 particles only occurs at higher temperatures (600-700ºC) than the heat treatment temperature applied in the present work (410ºC).

Changes in the nanoscale morphology are intimately related to changes in the specific surface area of the powder samples. While the TiNT specific surface area is 250-300 m^2/g, it decreases to 93 m^2/g after the thermal treatment at 410ºC due to dehydration, crystalline phase transformation, and the morphological conversion from nanotubes to nanorods [35]. Further modifications in the TiO_2 samples upon the insertion of carbon can also cause changes in their specific surfaces. Table 1 includes surface area values of the C/TiO_2 and SWCNT/C/TiO_2 materials with various carbon contents. For binary C/TiO_2 materials with low carbon contents, ranging from 0.3 to 1.2 wt.% C, surface areas are not substantially different from that of TiNRs without carbon. In fact, surface areas of the 25G-TiNR, 50G-TiNR and 100G-TiNR samples are between 74 and 99 m^2/g. On the contrary, surface areas clearly increase for C/TiO_2 materials with high carbon contents (> 5wt.% C), reaching values between 130 and 237 m^2/g (Table 1). This effect has been associated to the accumulation of porous carbon on TiO_2 surfaces [2]. When the carbon content is low, carbon atoms occupy sites within the TiO_2 crystalline structure. However, when the carbon content is high, carbon atoms are forced to migrate to the external surface, constituting porous structures. Partially graphitized layers on anatase TiO_2 crystals have been observed in C/TiO_2 composites prepared from electrochemically synthesized TiO_2 nanotubes and sucrose [7].

SWCNTs are low density and high specific surface nanostructures. Therefore, it is expected that ternary SWCNT/C/TiO_2 composites show higher specific surface areas than their corresponding binary C/TiO_2 composites and the TiNRs without carbon. In fact, surface areas for the SWCNT/C/TiO_2 composites were around 123-135 m^2/g, except for the Ox-SWCNT/100G-TiNR sample, which anomalously showed 82 m^2/g (Table 1). It can be concluded that the integration of SWCNTs usually produces a slight increase in the specific surface area. It should be pointed out that the amount of SWCNTs to be inserted in the composites was optimized in our previous study [33].

3.2 Crystallographic structure

It has been previously discussed that titanium oxide nanotubes (TiNTs) are converted into nanorods during the thermal treatment at 410ºC. The nanorods are not solid

monocrystalline nanostructures, but they are actually made of small anatase TiO_2 crystalline domains. Figure 2 shows the XRD patterns of binary C/TiNR composites with various carbon contents. All the diffractograms exhibit the characteristic features of anatase TiO_2. The peaks are quite broad, indicating small crystallite sizes. Anatase is the only TiO_2 crystalline phase present in the TiNRs, since no signals of brookite or rutile are detected by XRD. In fact, rutile usually forms at higher crystallization temperatures (>500ºC) [36]. The insertion of carbon in the C/TiNR binary composites do not induce new crystalline forms different from anatase. This fact is important, as C/TiO_2 composites synthesized by other methods may contain TiC crystals [3, 37-39]. For example, the characteristic peak of TiC at $2\theta \sim 36.1º$ has been detected in C/TiO_2 films prepared by spray pyrolysis and using glucose as the carbon precursor [38].

Crystallite sizes were calculated through the Scherrer equation for all the photocatalysts and they are listed in Table 1. Crystallite sizes ranged from 10 to 25 nm and were thus smaller than anatase crystallites in the standard photocatalyst Degussa P25. For C/TiNR binary composites, crystallite sizes slightly decreased as the carbon content increased. This fact could be associated to a decrease in the sample crystallinity due to carbon. The effect was noticeable when the carbon content was higher than 5wt.% and the specific surface area was higher than 130 m^2/g. Accumulation of carbon on the external surfaces of TiNRs could be hindering anatase crystal growth. Similarly, it has been reported that carbon coatings suppress rutile nucleation at high temperature [2].

The addition of SWCNTs for the preparation of ternary $SWCNT/C/TiO_2$ composites did not produce qualitative changes in the XRD patterns (diffractograms not shown). Since the ternary composites were prepared by physical mixture of C/TiNR binary composites and SWCNT dispersions, no modifications of the TiO_2 crystalline phase occurred. Anatase crystallite sizes in the ternary composites ranged from 12 to 22 nm. Crystallite sizes were smaller than those in their parental C/TiNR composites, except for the Ox-SWCNT/100G-TiNR sample (22 nm). This fact could be related to the partial collapse of nanorod structures during the physical mixture of C/TiNRs with the SWCNT dispersions. Actually, small crystallites were observed in the TEM images of ternary composites (Figure 1.d). It must be pointed here that the calculation of crystallite sizes was not influenced by the possible presence of additional carbon signals in the XRD patterns. For example, the intense anatase peak at $2\theta \sim 25.5º$ can broaden in the presence of the graphitic carbon peak at $2\theta \sim 26.5º$. In order to avoid errors in XRD

interpretation, various significant anatase signals were taken into account simultaneously in each pattern.

Additional information regarding the crystalline structure was obtained through Raman spectroscopy (Figure 3). All the photocatalyst samples showed the characteristic anatase bands at around 142 (E_g), 392 (B_{1g}), 513 (B_{1g}+A_g) and 636 (E_g) cm^{-1}. Spectra for binary C/TiNR composites with low carbon contents were similar to pure TiNRs, although the most intense anatase E_g band shifted from 142 to 156 cm^{-1}. For high carbon contents (400G-TiNR and 800G-TiNR samples) additional broad signals appeared at around 1350 and 1600 cm^{-1}, which can be respectively assigned to D and G bands of disordered carbon materials. This fact indicates a substantial accumulation of carbon on the TiO_2 external surfaces. The position of the 142 cm^{-1} anatase band further shifted to 163 cm^{-1} for the binary composites with high carbon contents. For ternary SWCNT/C/TiNR composites, the spectra showed broadened anatase signals and the resonant double G band of SWCNTs at around 1600 cm^{-1}. The intense E_g anatase band shifted to around 150 cm^{-1}.

3.3. The interaction between carbon and TiO_2

Doping is usually defined as the introduction of foreign elements in the host matrix without giving rise to a new crystallographic phase [25]. XPS measurements have been previously utilized to demonstrate carbon doping in C/TiNR binary composites [4]. As an example, Figure 4 includes the high resolution C 1s and valence band spectra of the 100G-TiNR material. The C 1s spectrum can be separated into two intense contributions at 285.4 and 284.5 eV, and two weak contributions at 290.6 and 282.2 eV. The contributions at 290.6, 285.4 and 284.5 eV have been respectively assigned to C=O, C-O, and C-C bonds, which can be originated from adventicious carbon [5]. The contribution at ~ 282.2 eV has been assigned to C-doped TiO_2, as it is near from the Ti-C bond energy [4,5,11,37,40].

The valence band XPS spectrum (Figure 4) has been proposed as a direct evidence of the TiO_2 band structure modification through carbon doping [4,5]. The spectrum profile represents the electronic density of states. The lowest level of the valence band appears at approximately 3.2 eV, just above the band-gap. Carbon doping causes the generation of energy levels inside the band-gap (at around 0-1 eV), which are responsible for the photoactivity under visible light. It must be noted here that XPS evidence of carbon doping (in both the C 1s and valence band regions) can only be obtained after Ar^+ ion

sputtering. The details regarding XPS characterization have been previously published [4, 5].

IR spectroscopy has been seldom applied to the characterization of the Ti-C interaction in C/TiO_2 composites, although signals at the region of low wavenumbers (400-1000 cm^{-1}), associated to Ti-O [41, 42] and Ti-C [43] bonds, are affected by thermal treatments and by the carbon content. Stretching of Ti-O-Ti bonds originates absorption bands between 500 and 900 cm^{-1}, and stretching of terminal Ti-O bonds in TiO_2 clusters is observed between 990 and 1033 cm^{-1} [42]. The spectrum of TiC nanocrystals is mainly defined by a strong resonance at 485 cm^{-1} and a secondary band at 600-700 cm^{-1} [43]. Figure 5 shows IR spectra of three pure titanium oxide samples: TiNTs, TiNRs and Degussa P25. All the spectra, which are background subtracted, show two moisture bands at ~ 3400 and 1630 cm^{-1}, as well as the Ti-O intense signal at 400-1000 cm^{-1}. Moisture bands of the TiNT sample are more intense than in the other two samples (TiNRs and P25 TiO_2), and the band at ~ 3400 cm^{-1} is much wider, ranging from 2400 to 3700 cm^{-1}. In fact, the water adsorption capacity of TiNTs is greater than that of TiNRs and P25 TiO_2 [35]. In addition, the TiNT material contains a large amount of crystallization water (or maybe OH intercalation groups), which is lost at temperatures higher than 150ºC [35], and could be responsible for the band broadening at 2400-3200 cm^{-1}.

The IR Ti-O band signal at low wavenumbers (400-1000 cm^{-1}) is quite different for each one of the three pure titanium oxide materials included in Figure 5 (TiNT, TiNR and P25). For the TiNT material, the Ti-O band shows three distinguishable components at 919, 672 and 496 cm^{-1}. However, the spectrum of TiNRs shows a wide band with its maximum at 595 cm^{-1}. It is clear that the thermal treatment applied for the conversion of the TiNT material into the TiNR produces a strong effect in the Ti-O band signal. For P25 TiO_2, the band shows a peak at 670 cm^{-1} with a shoulder at 506 cm^{-1}. Therefore, the Ti-O signal of P25, which is a material composed of anatase and rutile TiO_2, is quite different from that of TiNRs, which is only composed of anatase. It can be concluded that the IR band at low wavenumbers (400-1000 cm^{-1}) is highly sensitive to changes in Ti-O-Ti bond environment.

IR spectra of C/TiNR binary composites with various carbon contents are presented in Figure 6. Even a small amount of the glucose precursor produces modifications in the band at low wavenumbers (400-1000 cm^{-1}). The spectra of C/TiNRs show band maxima at 470-490 cm^{-1}, while the band maximum for pure TiNRs is at 594-650 cm^{-1}. For low

carbon content composites (50G-TiNR, 100G-TiNR), only the band at low wavenumbers is modified with respect to pure TiNRs, being the rest of the spectrum almost identical. However, spectra for high carbon content composites (400G-TiNR, 800G-TiNR) clearly show other features caused by the accumulation of carbon materials on the TiO_2 external surfaces. In fact, bands at 1100-1400 cm^{-1} and at ~ 1700 cm^{-1} are associated to oxygen bearing functional groups on carbon surfaces. Curve fitting of the band at low wavenumbers (400-100 cm^{-1}) clearly shows the presence of the strong Ti-C line at 488 cm^{-1} and also demonstrates a Ti-C contribution to the 664 cm^{-1} component. Moreover, the intensity of the Ti-C bands, particularly that between 500-600 cm^{-1}, decreases with increasing carbon contents, possibly due to the increasing TiC cluster size [43]. Thus, IR spectra of binary C/TiNR composites are consistent with carbon doping at low carbon contents, and clearly indicate the accumulation of carbon materials on the TiO_2 external surfaces for high glucose precursor levels. However, it must be remembered that the crystallographic structure is not modified in any case.

Figure 7 shows the IR spectra of the ternary composites (P-SWCNT/100G-TiNR and Ox-SWCNT/100G-TiNR) compared to their common parental 100G-TiNR binary composite. The three materials show moisture bands at 3410-3430 cm^{-1} and 1635 cm^{-1}, and their low-wavenumber bands present a maximum at 485 cm^{-1} due to the presence of Ti-C bonds. The band shape for the P-SWCNT/100G-TiNR composite is similar to the 100G-TiNR composite, although the relative intensity of its component at 485 cm^{-1} slightly decreases. The low-wavenumber band of the Ox-SWCNT/100G-TiNR composite, which was prepared with oxidized SWCNTs, shows a prominent shoulder at 675 cm^{-1}. This fact could indicate an interaction between the oxygen functional groups at SWCNT surfaces and TiO_2 crystallites, whose possible effect on the photocatalytic activity under visible light has been previously suggested [22].

The last part of this section is dedicated to visible light absorption properties of the composites. An interesting point is the direct observation of the material colors (Figure 8). While pure TiO_2 materials are white, the C/TiNR binary composites are gray. This fact does not result in an improved photoactivity, as it will be commented later. The C/TiNR color darkening can be understood as a progressive increase in the optical absorption at the visible range wavelengths (λ > 400 nm, Figure 8). Additionally, an increase in the λ-edge is observed at low carbon contents, in agreement with previously published results [4, 5]. For pure TiO_2 materials, the λ-edge is inversely proportional to the band-gap energy. However, for the C/TiNR materials, the λ-edge could be

influenced by the accumulation of black carbon materials at the outer TiO_2 surfaces, particularly at the highest carbon loadings. Therefore, the calculation of the band-gap energy from the absorbance spectrum is not considered here. All the ternary SWCNT/C/TiNR composites show high light absorption capacities in the entire visible region (Figure 8), due to the presence of carbon nanotubes. Similar spectra for binary CNT/TiO_2 composites have been previously reported [8].

3.4. Photocatalytic activity

The visible light photocatalytic activity of all the materials was tested for the decomposition of methylene blue in water solution. The results were interpreted in terms of a pseudo-first order kinetics. This procedure, which assumes a Langmuir-Hinshelwood mechanism for the degradation reactions, has been typically applied in the literature. The methylene blue concentration (C) in the solution is expressed as an exponential decay:

$$C = C_0 \exp(-kt)$$

where C_0 is the concentration of methylene blue after stirring with the catalyst in darkness for two hours, and k is the apparent first order rate constant.

The results of fitting experimental data to the first order kinetic model are shown in Figures 9-11. It can be observed that the kinetic model fits data well for times longer than approximately 30 min, but substantially deviates from the experimental points for short times. This phenomenon, which is quite often described in photocatalytic experiments, was already reported by Lettmann et al. [44] for C/TiO_2 composite photocatalysts. In that publication, the deviation at the initial times was associated to a partial deactivation of the photocatalyst during its first use. In fact, it was confirmed that photocatalytic experiments perfectly fitted the first order kinetic model in a second run utilizing a recycled photocatalyst. It was also demonstrated that the first order kinetic constant of the second (and following) cycles (k) can be calculated from the first cycle data, just allowing an independent term in the linear fitting of $\ln(C/C_0)$ vs. t:

$$\ln (C/C_0) = kt + \text{intercept}$$

This expression is applied instead of the first order kinetic model for the first photocatalytic cycle:

$$\ln(C/C_0) = k^0 t$$

where k^0 is the first cycle kinetic constant, which is different from the first order kinetic constant (k) for the second and following cycles. The calculated values of the first order

rate constant (k), the first cycle first order rate constant (k^0) and their corresponding regression coefficients (r^2) for all the samples studied are listed in Table 2. It can be generally observed that k constants are slightly lower than k^0 constants for the composite materials.

Figure 9 shows degradation kinetics for the series of binary C/TiNR photocatalysts with various carbon contents. The composites demonstrate substantial photocatalytic activities, while the activity of pure TiO_2 materials, such as P25 and TiNRs, is very low under visible light. Degradation rate strongly depends on the carbon content of the binary photocatalyst, obtaining the optimal performance with the 100G-TiNR sample (1.2 wt% C). At higher carbon contents, the photocatalytic efficiency decreases, indicating that accumulated carbon materials at the external TiO_2 surfaces prevent light from reaching the photocatalyst efficiently.

The effect of SWCNTs in the ternary SWCNT/C/TiNR composites can be observed in Figures 10 and 11. Figure 10 shows kinetic results for the ternary photocatalysts prepared from the parental 50G-TiNR binary composite, and Figure 11 includes the results for the photocatalysts prepared from the binary 100G-TiNR composite. The amount of SWCNT material in the ternary composites was of ~ 10wt% (Table 1), which is approximately the optimal value according to our previous experiments. Degradation rates for the ternary photocatalysts are slightly higher than for their parental binary composites (Table 2). The best result was obtained for the Ox-SWCNT/100G-TiNR material, which showed a rate constant of ~ 1.6 times higher than the 100G-TiNR photocatalyst. Reaction rates of the ternary photocatalysts prepared with oxidized SWCNTs were higher than those of the photocatalyst prepared with pristine SWCNTs. This effect could be associated to the improved purity of the Ox-SWCNTs or to the presence of oxygen functional groups at the surface of SWCNTs. It has been already pointed that oxygen functional groups on SWCNT surfaces can improve the photoactivity of SWCNT/TiO_2 composites through the interaction of the oxygen groups with the TiO_2 surface [22].

The ternary SWCNT/C/TiNR composites were prepared by physical mixture from the binary composites. While a thermal treatment was applied for the synthesis of binary C/TiNR composites, the materials were not annealed after mixing with SWCNTs. Therefore, the insertion of carbon atoms inside the TiO_2 network (carbon doping) could occur in the binary C/TiNR composites, but was not expected after mixing with SWCNTs. According to the literature, carbon in the C/TiNR binary composites acts as a

doping agent, and some C-Ti interactions are formed [4, 5]. The mechanism of the C/TiNR photocatalytic activity improvement under visible light can be explained by the formation of doping electronic states inside the TiO_2 bandgap [1]. However, SWCNTs do not perform as carbon doping sources, and the improvement in the photocatalytic activity can be associated to their properties as electron acceptors [33]. When SWCNTs are oxidized, an additional interaction could occur between TiO_2 and the SWCNT oxygen groups, although its mechanistic effect on the photocatalyst performance is not clear.

C/TiO_2 composite photocatalysts are quite complex systems, and many photochemical mechanisms have an influence in their performance. The total carbon content does not provide definitive information on the photocatalyst activity. The best binary photocatalyst in the present article was the 100G-TiNR material (1.2 wt% C), and the best photocatalyst was the Ox-SWCNT/100G-TiNR ternary composite (11.5 wt% C). The Ox-SWCNT/100G-TiNR material demonstrated a higher photoactivity than the 400G-TiNR material (13.0 wt% C), although their carbon contents were relatively close from each other. Clearly, different carbon forms are responsible for different photochemical mechanisms and processes.

4. Conclusions

Ternary $SWCNT/C/TiO_2$ composite photocatalysts were synthesized from hydrothermally produced titanium oxide nanotubes. During composite preparation, the initial nanotube morphology was converted into TiO_2 nanorods mixed with particles. TiO_2 nanorods were doped with carbon through a thermal treatment, using glucose as the precursor. Doping was confirmed by XPS and IR results. In addition, for high carbon content composites, excess carbon accumulated at the external TiO_2 surfaces. The TiO_2 crystallographic structure remained almost identical for all the composites, and TiO_2 anatase phase was identified by both XRD and Raman spectroscopy. Both doping with glucose and blending with SWCNTs produced a great increase in the visible light absorbance of TiO_2, which prevented an accurate calculation of the band gap energy from absorbance data.

The photocatalytic activity of binary C/TiNR composites under visible light was higher than that of pure TiO_2 (both TiNR and Degussa P25 materials), and the optimal C/TiNR photocatalyst (100G-TiNR) contained ~ 1 wt.% C. In addition, the photocatalytic activity of ternary $SWCNT/C/TiO_2$ materials was somewhat higher than that of binary

composites. The best results were obtained with the ternary Ox-SWCNT/100G-TiNR material, which was prepared with air-oxidized SWCNTs. The Ox-SWCNT/100G-TiNR and 400G-TiNR composites contained comparable amounts of total carbon; however, the former demonstrated a higher photocatalytic activity. This fact clearly indicates that the different carbon forms in the photocatalyst induce different synergistic mechanisms. According to the literature, it is suggested that heat treatment in glucose creates doping electronic states inside the TiO_2 band gap, while SWCNTs mainly act as electron withdrawers.

Acknowledgements

This work was funded by the Government of Aragon and "La Caixa" under project GA-LC-041/2008, the Spanish MINECO under the projects EUI2008-00152, TEC2010-15736, and PRI-PIBAR-2011-1, and the Government of Aragon (DGA) and the European Social Fund (ESF) under Project DGA-ESF-T66 CNN.

References

[1] R. Leary, A. Westwood, Carbonaceous nanomaterials for the enhancement of TiO_2 photocatalysis, Carbon 49 (2011) 741-772.

[2] M. Inagaki, F. Kojin, B. Tryba, M. Toyoda, Carbon-coated anatase: the role of the carbon layer for photocatalytic performance, Carbon 43 (2005) 1652-1659.

[3] Y. Cong, X. Li, Y. Qin, Z. Dong, G. Yuan, Z. Cui, X. Lai, Carbon-doped TiO_2 coating on multiwalled carbon nanotubes with higher visible light photocatalytic activity, Appl. Catal. B-Environmental 107 (2011) 128-134.

[4] Z. Wu, F. Dong, W. Zhao, H. Wang, The fabrication and characterization of novel carbon doped TiO_2 nanotubes, nanowires and nanorods with high visible light photocatalytic activity, Nanotechnology 20 (2009) 235701 (1-9).

[5] F. Dong, H. Wang, Z. Wu, One step "green" synthetic approach for mesoporous C-doped titanium dioxide with efficient visible light photocatalytic activity, J. Phys. Chem. C 113 (2009) 16717-16723.

[6] Y. Wang, J. Lin, R. Zong, J. He, Y. Zhu, Enhanced photoelectric catalytic degradation of methylene blue via TiO_2 nanotube arrays hybridized with graphite-like carbon, J. Mol. Catal. A-Chem. 349 (2011) 13-19.

[7] X. Lin, F. Rong, X. Ji, D. Fu, Carbon-doped mesoporous TiO_2 film and its photocatalytic activity. Micropor. Mesopor. Mater, 142 (2011) 276-281.

[8] W. Wang, P. Serp, P. Kalck, J.L. Faria, Visible light photodegradation of phenol on MWNT-TiO_2 composite catalysts prepared by a modified sol-gel method, J. Mol. Catal. A-Chem. 235 (2005) 194-199.

[9] X.H. Xia, Z.J. Jia, Y. Yu, Y. Liang, Z. Wang, L.L. Ma, Preparation of multi-walled carbon nanotube supported TiO_2 and its photocatalytic activity in the reduction of CO_2 with H_2O, Carbon 45 (2007) 717-721.

[10] K. Woan, G. Pyrgiotakis, W. Sigmund, Photocatalytic carbon-nanotube-TiO_2 composites, Adv. Mater. 21 (2009) 2233-2239.

[11] O. Akhavan, M. Abdolahad, Y. Abdi, S. Mohajerzadeh, Synthesis of titania/carbon nanotube heterojunction arrays for photoinactivation of E. Coli in visible light irradiation, Carbon 47 (2009) 3280-3287.

[12] G. Jiang, Z. Lin, L. Zhu, Y. Ding, H. Tang, Preparation and photoelectrocatalytic properties of titania/carbon nanotube composite films, Carbon 48 (2010) 3369-3375.

[13] C.G. Silva, J.L. Faria, Photocatalytic oxidation of benzene derivatives in aqueous suspensions: synergic effect induced by the introduction of carbon nanotubes in a TiO_2 matrix, Appl. Catal. B-Environ. 101 (2010) 81-89.

[14] J. Yu, T. Ma, S. Liu, Enhanced photocatalytic activity of mesoporous TiO_2 aggregates by embedding carbon nanotubes as electron-transfer channel, Phys. Chem. Chem. Phys. 13 (2011) 3491-3501.

[15] W. Chen, Z. Fan, B. Zhang, G. Ma, K. Takanabe, X. Zhang, Z. Lai, Enhanced visible-light activity of titania via confinement inside carbon nanotubes, J. Am. Chem. Soc. 133 (2011) 14896-14899.

[16] K. Zhang, F.J. Zhang, M.L. Chen, W.C. Oh, Comparison of catalytic activities for photocatalytic and sonocatalytic degradation of methylene blue in present of anatase TiO_2-CNT catalysts, Ultrason. Sonochem. 18 (2011) 765-772.

[17] C. Martinez, M. Canle, M.I. Fernandez, J.A. Santaballa, J. Faria, Aqueous degradation of diclofenac by heterogeneous photocatalysis using nanostructured materials, Appl. Catal. B-Environ. 107 (2011) 110-118.

[18] Z. Li, B. Gao, G. Z. Chen, R. Mokaya, S. Sotiropoulos, G.L. Puma, Carbon nanotube/titanium dioxide (CNT/TiO_2) core-shell nanocomposites with tailored shell thickness, CNT content and photocatalytic/photoelectrocatalytic properties, Appl. Catal. B-Environ. 110 (2011) 50-57.

[19] M.J. Sampaio, C.G. Silva, R.R.N. Marques, A.M.T. Silva, J.L. Faria, Carbon nanotube-TiO_2 thin films for photocatalytic applications, Catal. Today 161 (2011) 91-96.

[20] Y. Yao, G. Li, S. Ciston, R.W. Lueptow, K.A. Gray, Photoreactive TiO_2/carbon nanotube composites: synthesis and reactivity, Environ. Sci. Technol. 42 (2008) 4952-4957.

[21] T.T. Duong, Q.D. Nguyen, S.K. Hong, D. Kim, S.G. Yoon, T.H. Pham, Enhanced photoelectrochemical activity of the TiO_2/ITO nanocomposites grown onto single-walled carbon nanotubes at a low temperature by nanocluster deposition, Adv. Mater. 23 (2011) 5557-5562.

[22] B.K. Vijayan, N.M. Dimitrijevic, D. Finkelstein-Shapiro, J. Wu, K.A. Gray, Coupling titania nanotubes and carbon nanotubes to create photocatalytic nanocomposites, ACS Catal. 2 (2012) 223-229.

[23] L.M. Pastrana-Martinez, S. Morales-Torres, V. Likodimos, J.L. Figueiredo, J.L. Faria, P. Falaras, A.M.T. Silva, Advanced nanostructured photocatalysts base don reduced graphene oxide-TiO_2 composites for degradation of diphenhydramine pharmaceutical and methyl orange dye, Appl. Catal. B-Environ. 123-124 (2012) 241-256.

[24] Y. Zhang, Z.R. Tang, X. Fu, Y.J. Xu, Engineering the unique 2D mat of graphene to achieve graphene-TiO_2 nanocomposite for photocatalytic selective transformation: what advantage does graphene have over its forebear carbon nanotube?, ACS Nano 5 (2011) 7426-7435.

[25] W.Y. Teoh, J.A. Scott, R. Amal, Progress in heterogeneous photocatalysis: from classical radical chemistry to engineering nanomaterials and solar reactors, J. Phys. Chem. Lett. 3 (2012) 629-639.

[26] H. Kim, J. Kim, W. Kim, W. Choi, Enhanced photocatalytic and photoelectrochemical activity in the ternary hybrid of CdS/TiO_2/WO_3 through the cascadal electron transfer, J. Phys. Chem. C 115 (2011) 9797-9805.

[27] G. Yang, Z. Yan, T. Xiao, Preparation and characterization of SnO_2/ZnO/TiO_2 composite semiconductor with enhanced photocatalytic activity, Appl. Surf. Sci. 258 (2012) 8704-8712.

[28] T. Kasuga, M. Hiramatsu, A. Hoson, T. Sekino, K. Niihara, Titania nanotubes prepared by chemical processing, Adv. Mater. 11 (1999) 1307-1311.

[29] A. Anson-Casaos, J.M. Gonzalez-Dominguez, M.T. Martinez, Separation of single-walled carbon nanotubes from graphite by centrifugation in a surfactant or in polymer solutions, Carbon 48 (2010) 2917-2924.

[30] Y. Tan, D.E. Resasco, Dispersion of single-walled carbon nanotubes of narrow diameter distribution, J. Phys. Chem. B 109 (2005) 14454-14460.

[31] H. Cathcart, J.N. Coleman, Quantitative comparison of ultracentrifuged and diluted single walled nanotube dispersions; differences and dispersion quality, Chem. Phys. Lett. 474 (2009) 122-126.

[32] M.E. Itkis, D.E. Perea, S. Niyogi, S.M. Rickard, M.A. Hamon, H. Hu, B. Zhao, R.C. Haddon, Purity evaluation of as-prepared single-walled carbon nanotube soot by use of solution-phase near-IR spectroscopy, Nano Lett. 3 (2003) 309-314.

[33] I. Tacchini, E. Terrado, A. Ansón-Casaos, M.T. Martinez, SWCNTs as electron withdrawers in nanocrystalline anatase photocatalysts, Nano 7 (2012) 1250020.

[34] J. Qu, X.P. Gao, G.R. Li, Q.W. Jiang, T.Y. Yan, Structure transformation and photoelectrochemical properties of TiO_2 nanomaterials calcined from titanate nanotubes, J. Phys. Chem. C 113 (2009) 3359-3363.

[35] I. Tacchini, A. Anson-Casaos, Y. Yu, M.T. Martinez, M. Lira-Cantu, Hydrothermal synthesis of 1D TiO_2 nanostructures for dye sensitized solar cells, Mater. Sci. Eng. B 177 (2011) 19-26.

[36] C.G. Silva, J.L. Faria, Anatase vs. rutile efficiency on the photocatalytic degradation of clofibric acid under near UV to visible irradiation, Photochem. Photobiol. Sci. 8 (2009) 705-711.

[37] Y. Choi, T. Umebayashi, M. Yoshikawa, Fabrication and characterization of C-doped anatase TiO_2 photocatalysts, J. Mater. Sci. 39 (2004), 1837-1839.

[38] C. Xu, R. Killmeyer, M.L. Gray, S.U.M. Khan, Enhanced carbon doping of n-TiO_2 thin films for photoelectrochemical water splitting, Electrochem. Commun. 8 (2006) 1650-1654.

[39] H. Wang, X. Quan, H. Yu, S. Chen, Fabrication of a TiO_2/carbon nanowall heterojunction and its photocatalytic ability, Carbon 46 (2008) 1126-1132.

[40] H. Irie, S. Washizuka, K. Hashimoto, Hydrophilicity on carbon-doped TiO_2 thin films under visible light, Thin Solid Films, 510 (2006) 21-25.

[41] T. Lopez, E. Sanchez, P. Bosch, Y. Meas, R. Gomez, FTIR and UV-Vis (diffuse reflectance) spectroscopic characterization of TiO_2 sol-gel, Mater. Chem. Phys. 32 (1992) 141-152.

[42] Z.W. Qu, G.J. Kroes, Theoretical study of the electronic structure and stability of titanium dioxide clusters $(TiO_2)_n$ with n = 1-9, J. Phys. Chem. B 110 (2006) 8998-9007.
[43] M. Patzschke, D. Sundholm, Density-Functional-Theory studies of the infrared spectra of titanium carbide nanocrystals, J. Phys. Chem. B 109 (2005) 12503-12508.
[44] C. Lettmann, K. Hildenbrand, H. Kisch, W. Macyk, W.F. Maier, Visible light photodegradation of 4-chlorophenol with a coke-containing titanium dioxide photocatalyst, Appl. Catal. B-Environ. 32 (2001) 215-227.

Table 1. Carbon content, specific surface area (S_{BET}) and crystallite size (χ_c) for all the samples studied.

Sample	C [Wt.%]	S_{BET} [m^2/g]	χ_c [nm]
P25	0	50	32A/52R[a]
TiNR	0	93	21
25G-TiNR	0.3	99	22
50G-TiNR	0.5	74	24
100G-TiNR	1.2	84	21
200G-TiNR	5.2	130	17
400G-TiNR	13.0	183	10
800G-TiNR	25.4	237	12
P-SWCNT/50G-TiNR	10.1	134	12
Ox-SWCNT/50G-TiNR	9.7	134	13
P-SWCNT/100G-TiNR	11.2	123	14
Ox-SWCNT/100G-TiNR	11.5	82	22

[a]Sizes of the anatase (A) and rutile (R) crystallites, respectively.

Table 2. First order rate constant (k), first cycle first order rate constant (k^0) and their corresponding regression coefficients (r^2) for all the samples studied.

Sample	k [min^{-1}]	r^2	k^0 [min^{-1}]	r^2
P25	0.0006	0.989	0.0006	0.985
TiNR	0.0006	0.985	0.0006	0.984
25G-TiNR	0.0115	0.993	0.0130	0.966
50G-TiNR	0.0138	0.993	0.0144	0.991
100G-TiNR	0.0208	0.993	0.0241	0.958
200G-TiNR	0.0116	0.987	0.0115	0.987
400G-TiNR	0.0070	0.998	0.0071	0.998
800G-TiNR	0.0050	0.987	0.0049	0.986
P-SWCNT/50G-TiNR	0.0152	0.992	0.0173	0.967
Ox-SWCNT/50G-TiNR	0.0171	0.995	0.0187	0.981
P-SWCNT/100G-TiNR	0.0246	0.993	0.0282	0.962
Ox-SWCNT/100G-TiNR	0.0325	0.999	0.0360	0.983

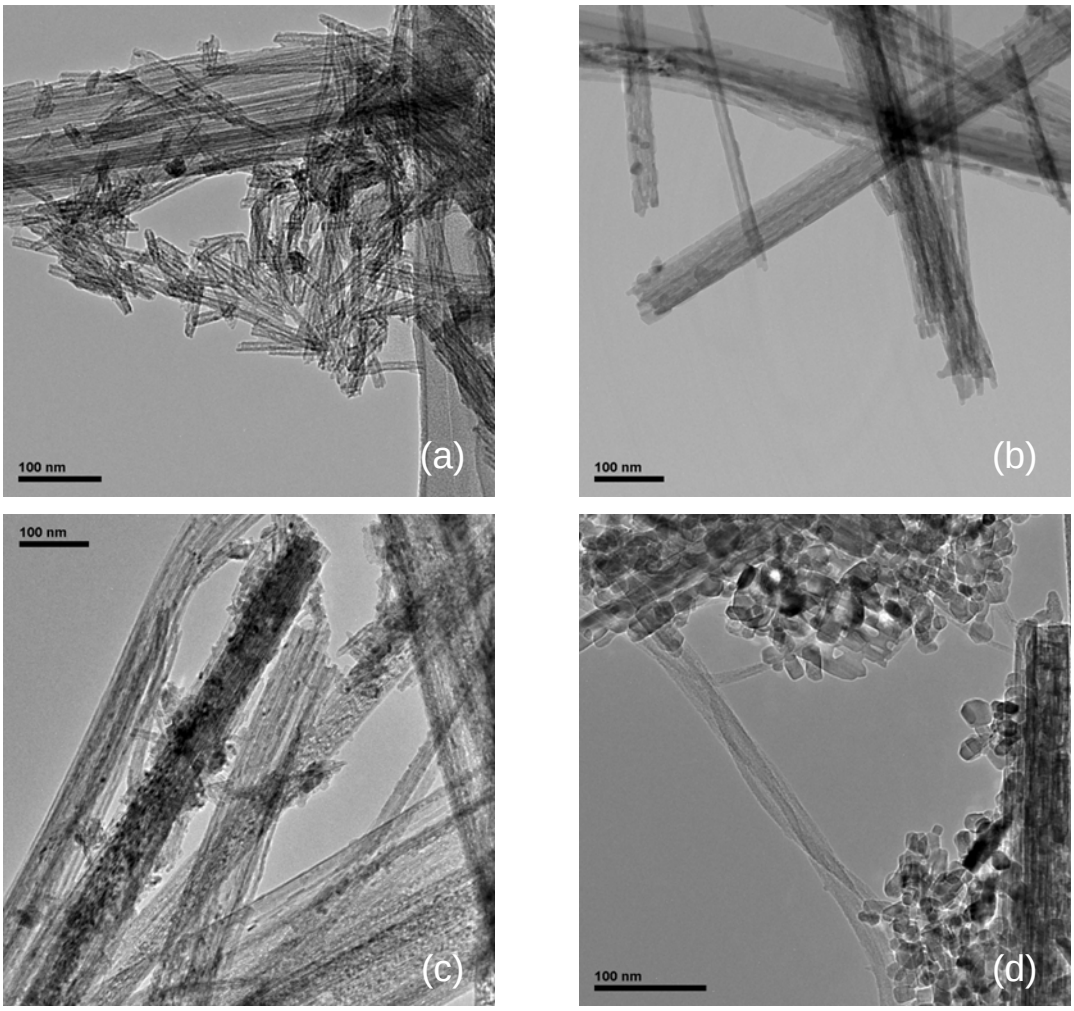

Figure 1. TEM images of a) TiNT, b) TiNR, c) 100G-TiNR, d) Ox-SWCNT/100G-TiNR.

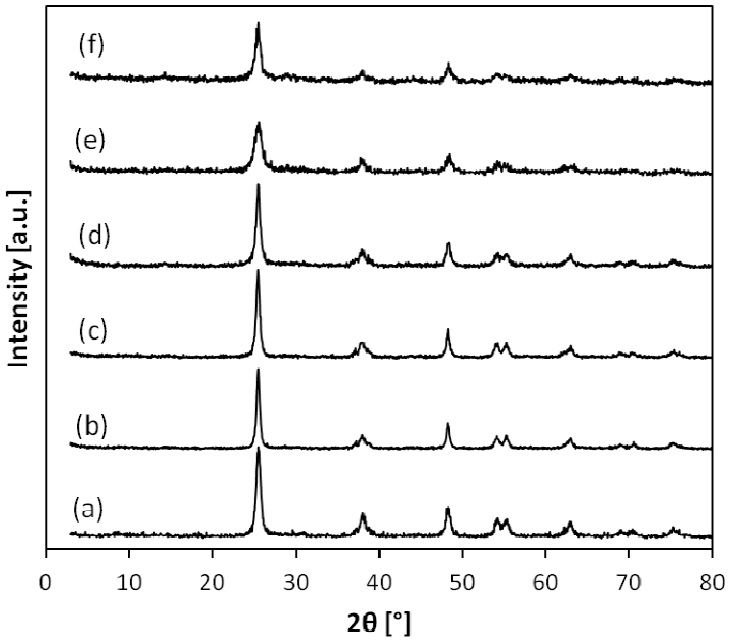

Figure 2. XRD patterns for a) 25G-TiNR, b) 50G-TiNR, c) 100G-TiNR, d) 200G-TiNR, e) 400G-TiNR and f) 800G-TiNR.

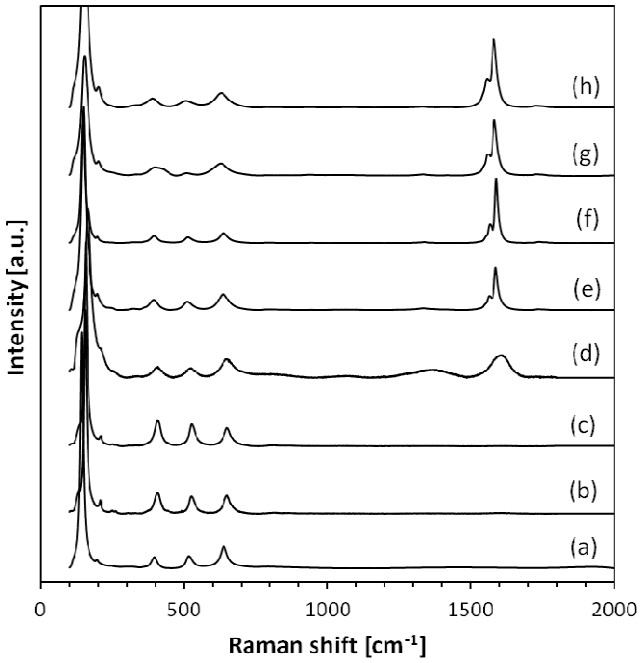

Figure 3. Raman spectra of a) TiNR, b) 50G-TiNR, c) 100G-TiNR, d) 400G-TiNR, e) P-SWCNT/50G-TiNR, f) Ox-SWCNT/50G-TiNR, g) P-SWCNT/100G-TiNR and h) Ox-SWCNT/100G-TiNR.

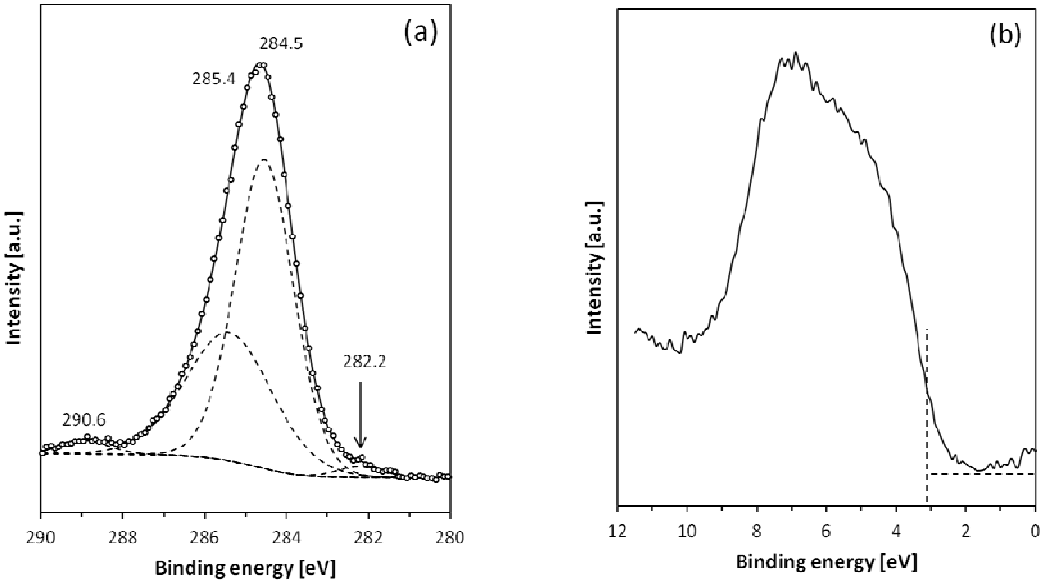

Figure 4. High resolution C 1s (a) and valence band (b) XPS spectra of the 100G-TiNR photocatalyst.

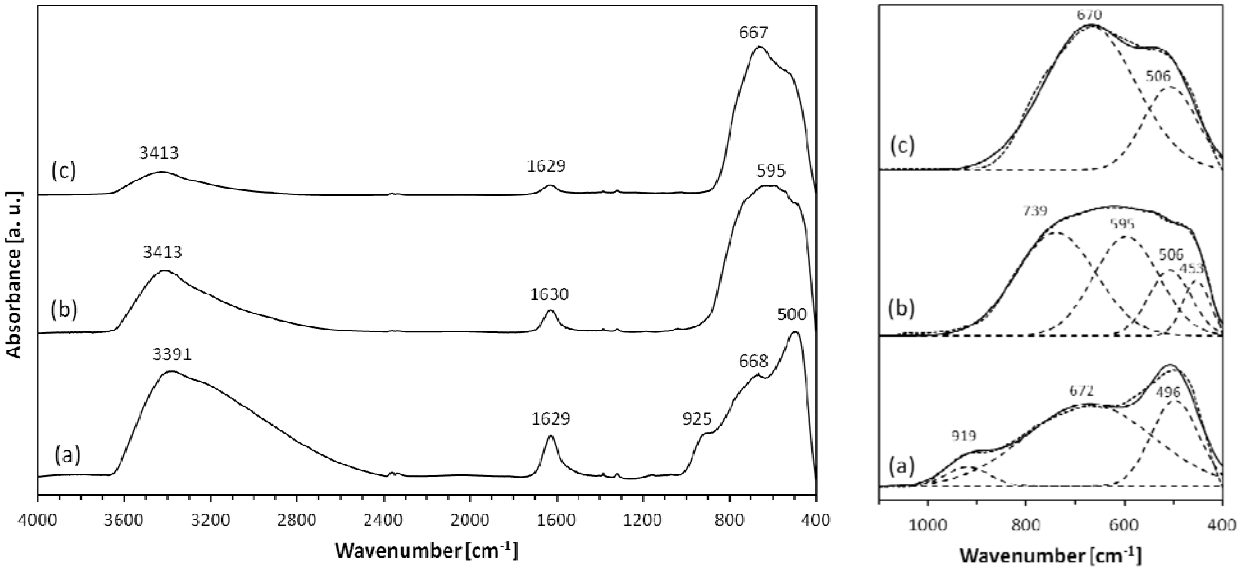

Figure 5. IR spectra of a) TiNT, b) TiNR and c) P25 TiO_2. The right panel includes the minimum number of Gaussian components needed to fit the band between 400 and 1100 cm^{-1}.

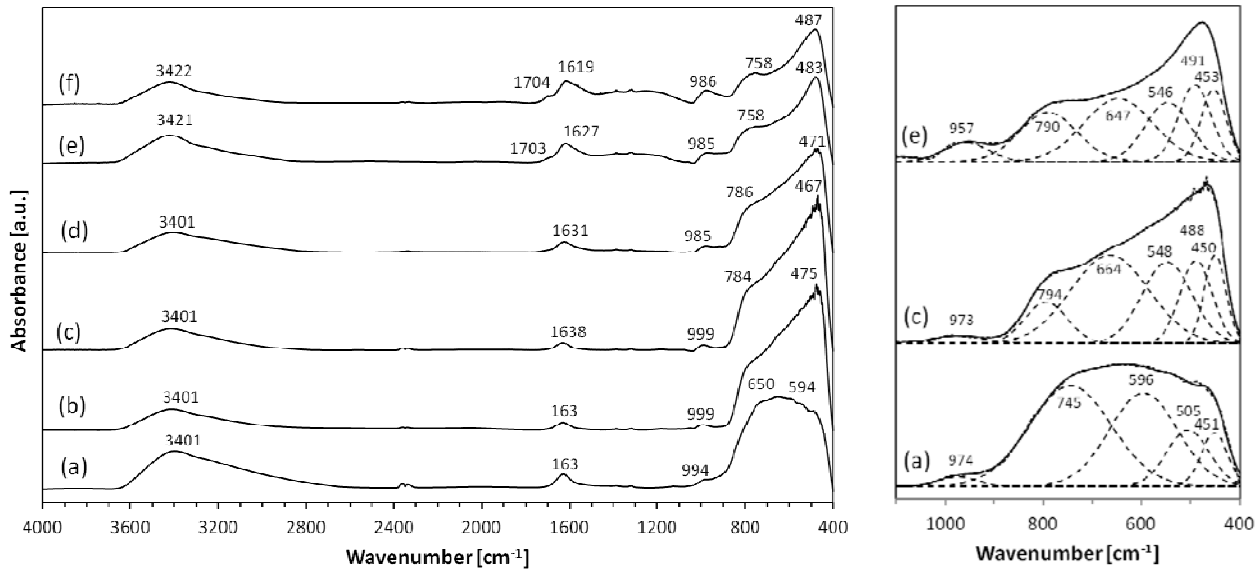

Figure 6. IR spectra of a) TiNR, b) 50G-TiNR, c) 100G-TiNR, d) 200G-TiNR, e) 400G-TiNR and f) 800G-TiNR. The right panel includes the minimum number of Gaussian components needed to fit the band between 400 and 1100 cm^{-1}.

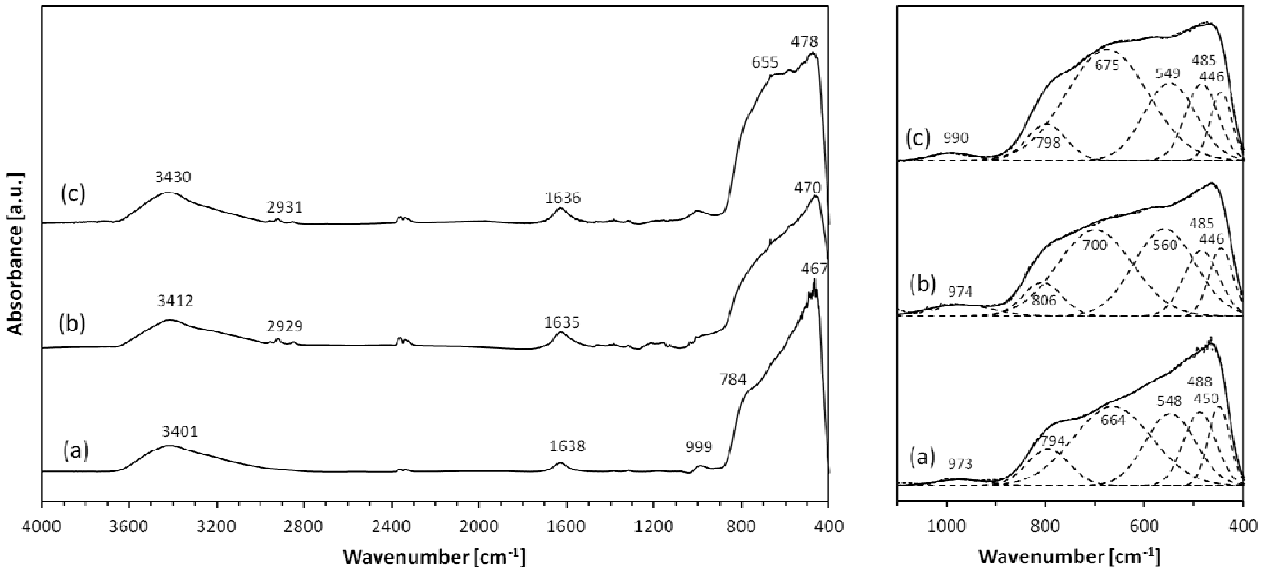

Figure 7. IR spectra of a) 100G-TiNR, b) P-SWCNT/100G-TiNR and c) Ox-SWCNT/100G-TiNR. The right panel includes the minimum number of Gaussian components needed to fit the band between 400 and 1100 cm^{-1}.

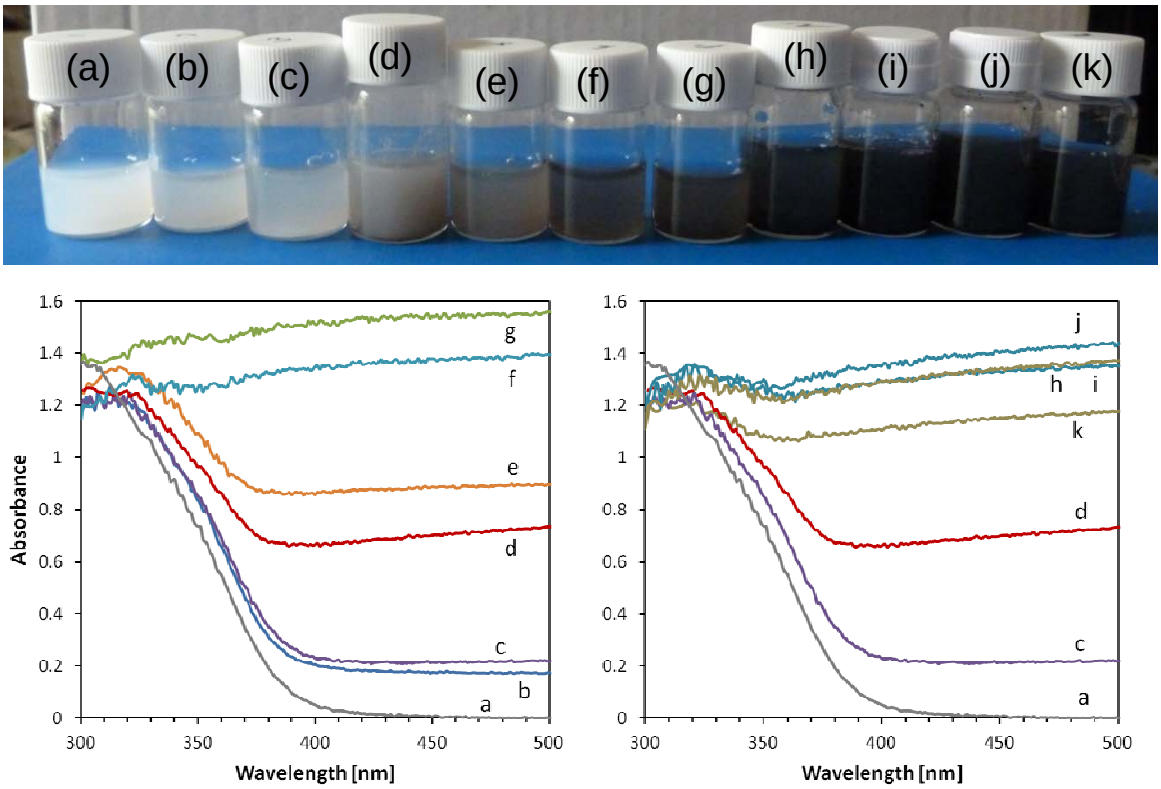

Figure 8. Photograph of the aqueous suspensions and UV-visible spectra of the solid photocatalyst powders: a) TiNR, b) 25G-TiNR, c) 50G-TiNR, d) 100G-TiNR, e) 200G-TiNR, f) 400G-TiNR, g) 800G-TiNR, h) P-SWCNT/50G-TiNR, i) Ox-SWCNT/50G-TiNR, j) P-SWCNT/100G-TiNR, k) Ox-SWCNT/100G-TiNR.

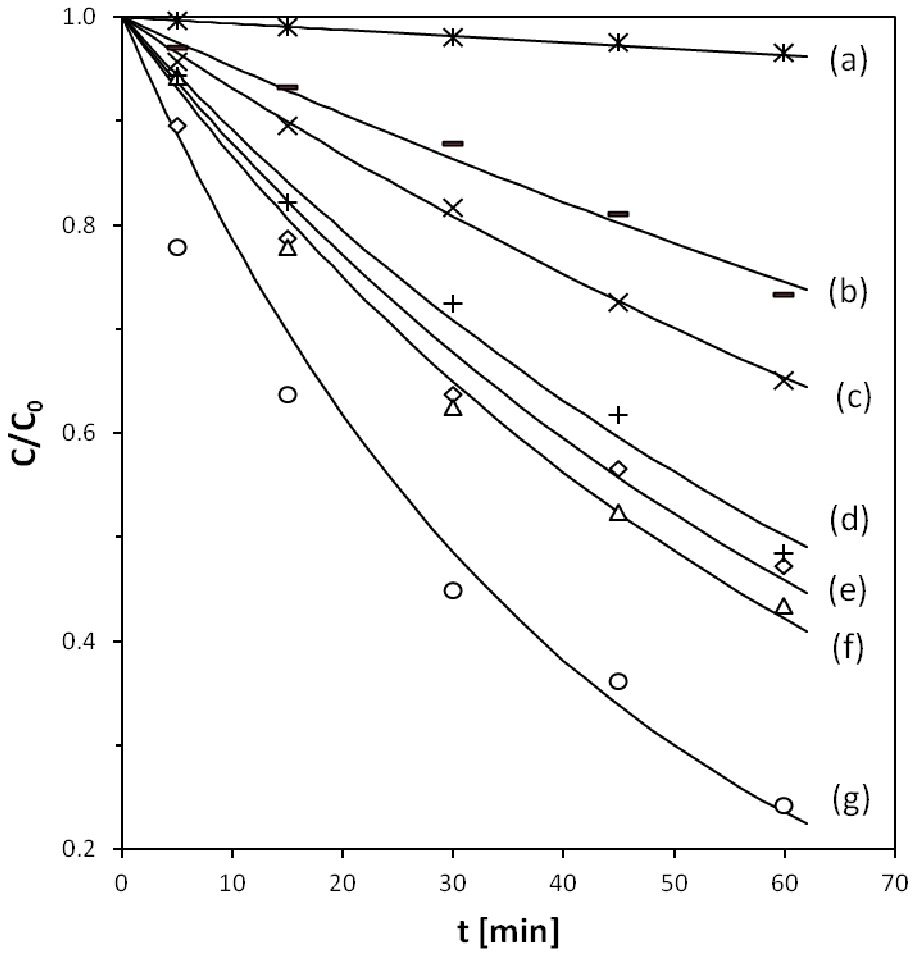

Figure 9. Photocatalytic degradation of methylene blue under visible light in the presence of: a) P25 TiO_2, b) 800G-TiNR, c) 400G-TiNR, d) 200G-TiNR, e) 25G-TiNR, f) 50G-TiNR, and g) 100G-TiNR.

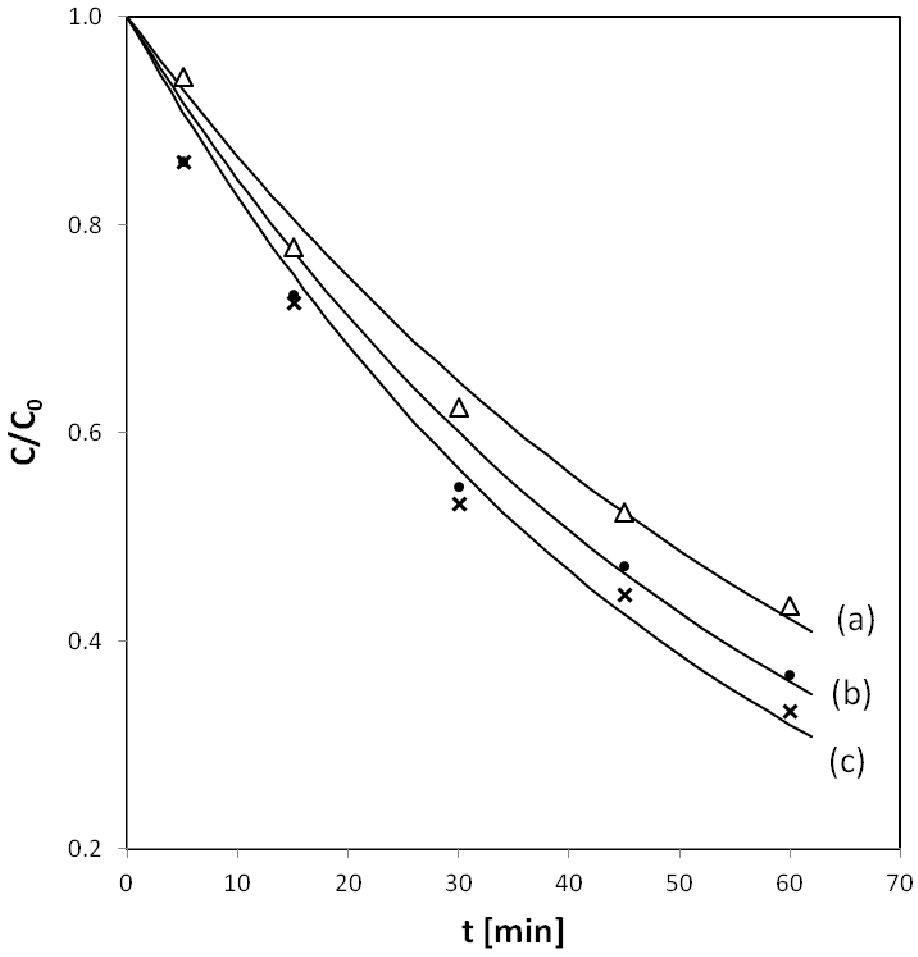

Figure 10. Photocatalytic degradation of methylene blue under visible light in the presence of: a) 50G-TiNR, b) P-SWCNT/50G-TiNR, and c) Ox-SWCNT/50G-TiNR

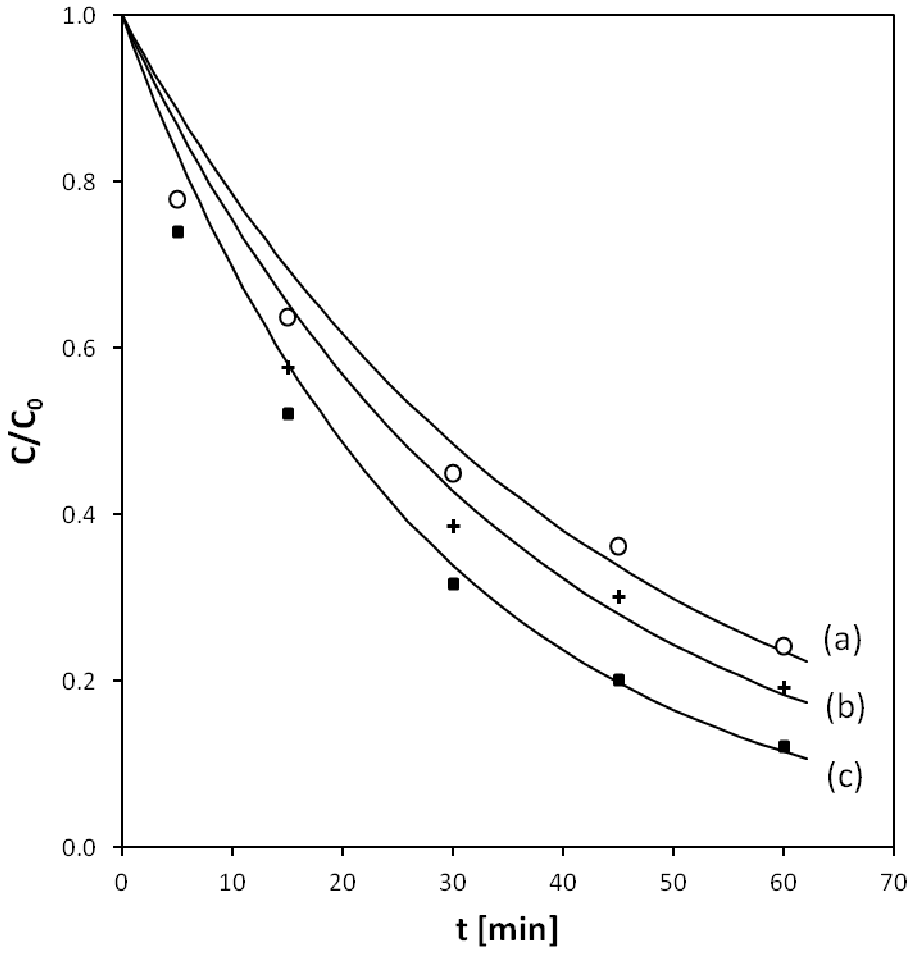

Figure 11. Photocatalytic degradation of methylene blue under visible light in the presence of: a) 100G-TiNR, b) P-SWCNT/100G-TiNR, and c) Ox-SWCNT/100G-TiNR.